

Interannual variations in the atmospheric heat budget

Kevin E. Trenberth, David P. Stepaniak, and Julie M. Caron

National Center for Atmospheric Research, Boulder, Colorado, USA

Received 27 December 2000; revised 29 August 2001; accepted 5 September 2001; published 24 April 2002.

[1] Interannual variability of the atmospheric heat budget is explored via a new data set of the computed vertically integrated energy transports to examine relationships with other fields. A case study reveals very large monthly divergences of these transports regionally with El Niño-Southern Oscillation (ENSO) and the associated changes with the Pacific-North American teleconnection pattern, and with the North Atlantic Oscillation. In the tropical Pacific during large El Niño events the anomalous divergence of the atmospheric energy transports exceeds 50 W m^{-2} over broad regions for several months. Examination of the corresponding top-of-the-atmosphere net radiative fluxes shows that it is primarily the surface fluxes from the ocean to the atmosphere that feed the divergent atmospheric transports. A systematic investigation of the covariability of sea surface temperatures (SSTs) and the divergence of atmospheric energy transport, using singular value decomposition analysis of the temporal covariance, reveals ENSO as dominant in the first two modes, explaining 62% and 12% of the covariance in the Pacific domain and explaining 39.5% and 15.4% globally for the first and second modes, respectively. The first mode is well represented by the time series for the SST index for Niño 3.4 region ($170^{\circ}\text{W}-120^{\circ}\text{W}, 5^{\circ}\text{N}-5^{\circ}\text{S}$). Regression analysis allows a more complete view of how the SSTs, outgoing longwave radiation, precipitation, diabatic heating, and atmospheric circulation respond with ENSO. The second mode indicates aspects of the systematic evolution of ENSO with time, with strong lead and lag correlations. It primarily reflects differences in the evolution of ENSO across the tropical Pacific from about the dateline to coastal South America. High SSTs associated with warm ENSO events are damped through surface heat fluxes into the atmosphere, which transports the energy into higher latitudes and throughout the tropics, contributing to loss of heat by the ocean, while the cold ENSO events correspond to a recharge phase as heat enters the ocean. Diabatic processes are clearly important within ENSO evolution. *INDEX TERMS:* 1620 Global Change: Climate dynamics (3309); 4215 Oceanography: General: Climate and interannual variability (3309); 4522 Oceanography: Physical: El Niño; 3309 Meteorology and Atmospheric Dynamics: Climatology (1620); *KEYWORDS:* heat budget, ENSO, radiation budget, climate variability, sea surface temperatures, atmospheric energy

1. Introduction

[2] It is widely accepted that persistent climate anomalies arise primarily from interactions of the atmosphere with other components of the climate system because the heat capacity of the atmosphere is small and equivalent to that of only $\sim 3.1 \text{ m}$ of the ocean (factoring in the 70% or so ocean coverage of the planet). Accordingly, a key forcing of atmospheric climate variability on all timescales is through the surface fluxes of heat, moisture, and momentum. Because conduction of heat is small, the masses of land and ice sheets involved in climate variability on interannual and decadal timescales are very small, and the main role of land is through variations in moisture storage and supply. Consequently, the main actively varying heat sources and sinks for the atmosphere are the oceans and sea ice, where turbulent exchanges play key roles.

[3] The sea surface temperature (SST) field is a key field in the two-way communication between the atmosphere and ocean. To the extent that SST anomalies persist, they have to be supported by a substantial heat content anomaly of the ocean mixed layer, especially if they are to have an influence on the atmosphere. Such an influence typically means that the anomalous heat is being drained from the ocean and thus a negative feedback occurs, as seems to be the case generally in the tropics

[Barnett *et al.*, 1991]. Aside from having a large reservoir to call upon in the ocean, an alternative way in which persistent climate anomalies can develop is if the atmosphere-ocean evolves as a coupled system, as occurs in El Niño-Southern Oscillation (ENSO).

[4] In this paper we explore contemporary variations in the global atmospheric heat budget through the divergent component of the atmospheric energy transports and through their relationship to the SST field. A number of data sets are employed, as given in section 2. In section 3 we first show some intriguing anomalies in a case study of two January months that were very different in both the phase of ENSO and in the North Atlantic Oscillation (NAO). In section 4 we then explore the time sequences in the tropical Pacific and expand to the global domain through a singular value decomposition (SVD) analysis of the cross-covariance matrix between SST and the divergence of atmospheric energy, along with precipitation as a key indicator of the latent heating of the tropical atmosphere, outgoing longwave radiation (OLR), and estimates of the atmospheric diabatic heating. In this way we attempt to clarify the role of surface fluxes and diabatic processes and how they relate to SST variations. We show that at least two indices are needed to characterize ENSO variability, and we propose a new index to help do so. Results hint strongly at significant lead and lag relationships that are related to the slow evolution of ENSO, but these are explored elsewhere. The consistency of results from the different data sets is discussed in section 5, and the conclusions are given in section 6.

2. Data and Methods

[5] Key data sets consist of a number of monthly mean derived products from the atmospheric reanalyses from the National Centers for Environmental Prediction/National Center for Atmospheric Research (NCEP/NCAR) and the European Centre for Medium-Range Weather Forecasts (ECMWF), as described by Trenberth *et al.* [2001a], for the period 1979–1993 for ECMWF and 1979–1998 for NCEP (however, see Appendix A for some recent reprocessing). The full-resolution atmospheric reanalyses, four times daily, on model coordinates were used to obtain the best accuracy possible for the atmospheric transports. The mass budget was first utilized as a constraint, and adjustments are made to the vertically integrated mass flows to ensure a mass balance on a monthly mean basis. Then we computed for each month the vertically integrated total atmospheric energy transports F_A and their divergence $\nabla \cdot F_A$. Diabatic heating is computed as a residual from the thermodynamic equation [Trenberth and Solomon, 1994]. The vertically integrated moisture transports and other quantities were also computed. The total energy consists of the potential and internal energy, the latent energy, and the kinetic energy, while the transports also include a pressure-work term so that the transport can be broken down into components from the dry static energy and the moist (or latent) component, which together make up the moist static energy, plus the kinetic energy. In addition, we compute the tendencies in mass and atmospheric energy storage utilizing values at the beginning and end of each month. The energy tendencies are combined with the computed divergence of the vertically integrated atmospheric energy transports to give the net column change, which has to be balanced by the top-of-the-atmosphere (TOA) radiation R_T and/or the surface fluxes F_s ; see Trenberth and Solomon [1994] and Trenberth *et al.* [2001a] for details. Ignoring the tendencies in storage, which are small,

$$\nabla \cdot F_A = R_T + F_s, \quad (1)$$

where F_s is directed upward and R_T is directed downward. Over the oceans in the extratropics, Trenberth *et al.* [2001a] evaluate and compare results from the two reanalyses and show that they agree in their monthly mean anomaly time series with correlations exceeding 0.6 for the vertically integrated total energy divergence. The agreement is not as good in the tropics. Local errors of $\sim 25\text{--}30 \text{ W m}^{-2}$ on T31 scales ($\sim 500 \text{ km}$) are inferred in most places, although embedded within a signal of $\sim 40 \text{ W m}^{-2}$ in the extratropics for monthly anomalies. Note that the derived quantity is a divergence, which is zero when spatially averaged globally, and it typically has a “blue” spatial power spectrum, with increasing power with higher wave number. Accordingly, spatial and temporal averaging reduces the above errors, and the systematic errors are much less than in other approaches (e.g., where the surface fluxes are estimated from parameterizations [Trenberth *et al.*, 2001a]). We exploit the large spatial and temporal scales of ENSO to bring out the ENSO signal from the noise.

[6] However, continuity problems with the ECMWF reanalyses arising from the positive reinforcement of biases in satellite radiances with those of the assimilating model first guess [Stendel *et al.*, 2000; Trenberth *et al.*, 2001b] undermine their utility for exploring climate variability. In addition, the implied ocean heat transports from the ECMWF reanalyses do not agree within error bars of direct oceanographic estimates whereas those from NCEP/NCAR do [Trenberth and Caron, 2001]. The time series of tropical temperatures from the NCEP reanalyses also appear to be more consistent. Accordingly, we use the NCEP-derived products to explore aspects of interannual variability.

[7] Net surface fluxes from the ocean into the atmosphere can therefore be computed from (1) only when reliable net TOA radiation data are available, such as during the Earth Radiation Budget Experiment (ERBE). This method avoids the substantial

biases and uncertainties associated with bulk flux formulations and spatial and temporal sampling and is physically consistent with the global constraints. It is limited by the accuracy of especially the atmospheric energy transports, which have been extensively evaluated by Trenberth *et al.* [2001a] and Trenberth and Caron [2001]. The availability of satellite radiation data can be seen in Figure 9 (presented later). ERBE data are available from February 1985 to April 1989, but we will also refer to results when we have only the atmospheric energy divergence available. The root-mean-square (RMS) uncertainty in net TOA radiation is estimated [Rieland and Raschke, 1991] to be 7.8 W m^{-2} for the three-satellite combination of ERBE versus 11 W m^{-2} for one satellite, with larger uncertainty in the absorbed solar radiation (ASR). The ERBE data contain discontinuities when the NOAA 9 satellite was lost, and we have adjusted the data set to accommodate this. We have also filled in missing data, which are pervasive near the delimiter of the solar radiation. Trenberth [1997] describes the methods, changes, and availability of the revised ERBE data set (available at www.cgd.ucar.edu/cas/catalog/satellite/erbe/).

[8] In 1998, new TOA radiation fluxes became available from Clouds and the Earth’s Radiant Energy System (CERES) instruments on the Tropical Rainfall Measurement Mission (TRMM) for the region equatorward of $\sim 40^\circ$ latitude. These fluxes are being evaluated to ensure their compatibility with earlier measurements, and results thus far [e.g., Wielicki *et al.*, 1999] suggest good comparability, and so we will make cautious use of some of these as well. TRMM precesses through all local hours of the day every 23 days, and this can lead to noise and aliasing of the diurnal cycle onto monthly means. Because 23 days is close to two-thirds of a month, the diurnal cycle aliases onto 3-monthly periods when using monthly means, with $\sim 21\%$ of the amplitude, so that monthly data should be noisy with spurious variance at 3-month periods.

[9] Nimbus 7 wide field of view data exist from 1979 through October 1987 and have been compared with ERBE data by Kyle *et al.* [1990]. There are some modest biases shown to exist. For the common period, we have computed the climatologies of each and then taken the anomalies from all the Nimbus 7 data sets and added them onto the ERBE means to provide an adjusted Nimbus 7 data set that is more consistent with that from ERBE than the raw data. The wide field of view active cavity radiometer on Nimbus 7 has a footprint of $1000\text{--}2000 \text{ km}$ across, and thus radiation measurements are less accurate regionally. In addition, while the Nimbus 7 orbit remained stable for several years, it began to precess after about 1986, changing the time of day of the observation, see Kyle *et al.* [1993] for details on the data. It is possible that some spurious low-frequency trends arise from drift in the zero level of the cavity radiometer. Some low-frequency trends in the data set are therefore probably not physical. Also, a sharp discontinuity about November 1980 may have arisen from changes in algorithms used in the data processing necessitated by problems in channels 12 and 13 [Kyle *et al.*, 1993].

[10] We also make use of the OLR data set from the National Oceanic and Atmospheric Administration (NOAA) series of satellites. However, the OLR contains inhomogeneities associated with different satellites and their different equatorial crossing times and orbital drift, and we use a version for which some of these have been adjusted with results from Waliser and Zhou [1997]. We apply the correction to the region between $\sim \pm 30^\circ$ (through July 1996 only) and taper the correction to zero near $\pm 30^\circ$ to smooth any discontinuities that might be introduced: the region between $\pm 27.5^\circ$ latitude is fully corrected; the correction at $\pm 30^\circ$ is weighted two thirds and also applied at $\pm 32.5^\circ$ with one-third weight. There is no correction poleward of 32.5° .

[11] We use the SSTs from NCEP from the optimal interpolation SST analysis of Reynolds and Smith [1994] after 1982, and we use the empirical orthogonal function reconstructed SST analysis of Smith *et al.* [1996] for the period before then. The latter does not

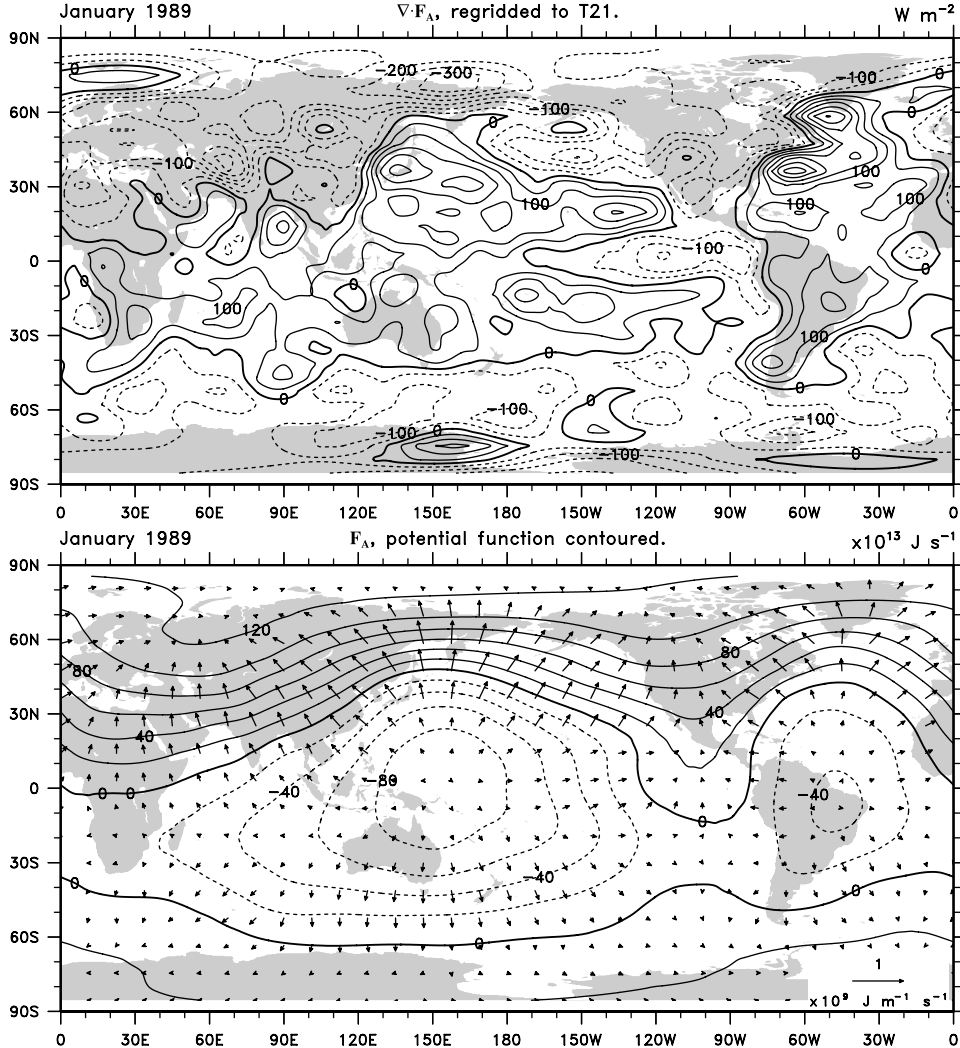


Figure 1. Total divergent vertically integrated energy transport and its divergence for January 1989. (top) Divergence of the transport truncated at T21 in watts per square meter. Contour interval is 50 W m^{-2} . (bottom) Transport in 10^{13} joules per second along with its potential function. Negative values are shown as dashed contours. If the top-of-the-atmosphere (TOA) radiation is unchanged, then positive values indicate a flux out of the ocean.

contain anomalies south of 40°S . However, these SSTs are preferred to those in the global surface temperature data set from the University of East Anglia and the United Kingdom Meteorological Office [Hurrell and Trenberth, 1999], which is also employed to examine values over land. We also utilize the precipitation data set from Xie and Arkin [1996, 1997], called the Climate Prediction Center (CPC) Merged Analysis of Precipitation (CMAP). Over land these fields are mainly based on information from rain gauge observations, while over the ocean they primarily use satellite estimates made with several different algorithms based on OLR and scattering and emission of microwave radiation.

[12] Various exploratory analyses, including empirical orthogonal function analysis, have been employed, but the results deemed most enlightening have arisen from singular value decomposition (SVD) of the cross-covariance matrix between two variables [Bretherton et al., 1992], such as SST with the divergence of atmospheric energy, and of both of those fields with OLR and precipitation. In addition, we employ correlation and regression analysis to help define relationships. Because large natural variability on synoptic timescales appears as weather noise in monthly means and because spurious noise related to sampling is also present (especially for SSTs, OLR, and net radiation), we have

smoothed the monthly anomaly fields used in the SVD analyses with a binomial one-quarter (1, 2, 1) filter, which removes two-month fluctuations.

[13] SVD analysis brings out the spatial patterns and their associated time series (or expansion coefficients) that explain the maximal mean square temporal covariance between two fields. We use monthly mean fields that have been normalized by their standard deviation. One variable is designated the “left” field and one is the “right” field. As well as obtaining the total squared covariance fraction (SCF) explained by the modes resulting from the analysis, we also obtain the correlation between the two time series for each mode as a measure of how well they agree. The modes are ordered by SCF ranking. Correlation or regression of the left (right) time series with the left (right) field provides what is called the “homogeneous” patterns associated with each mode, while correlations and regressions with the opposite right (left) field provide the “heterogeneous” patterns. When the correlations between the time series are high, there is very little difference between the homogeneous and heterogeneous patterns, although the former are naturally stronger. However, the heterogeneous patterns are appropriate in order to judge the response of one field to the other.

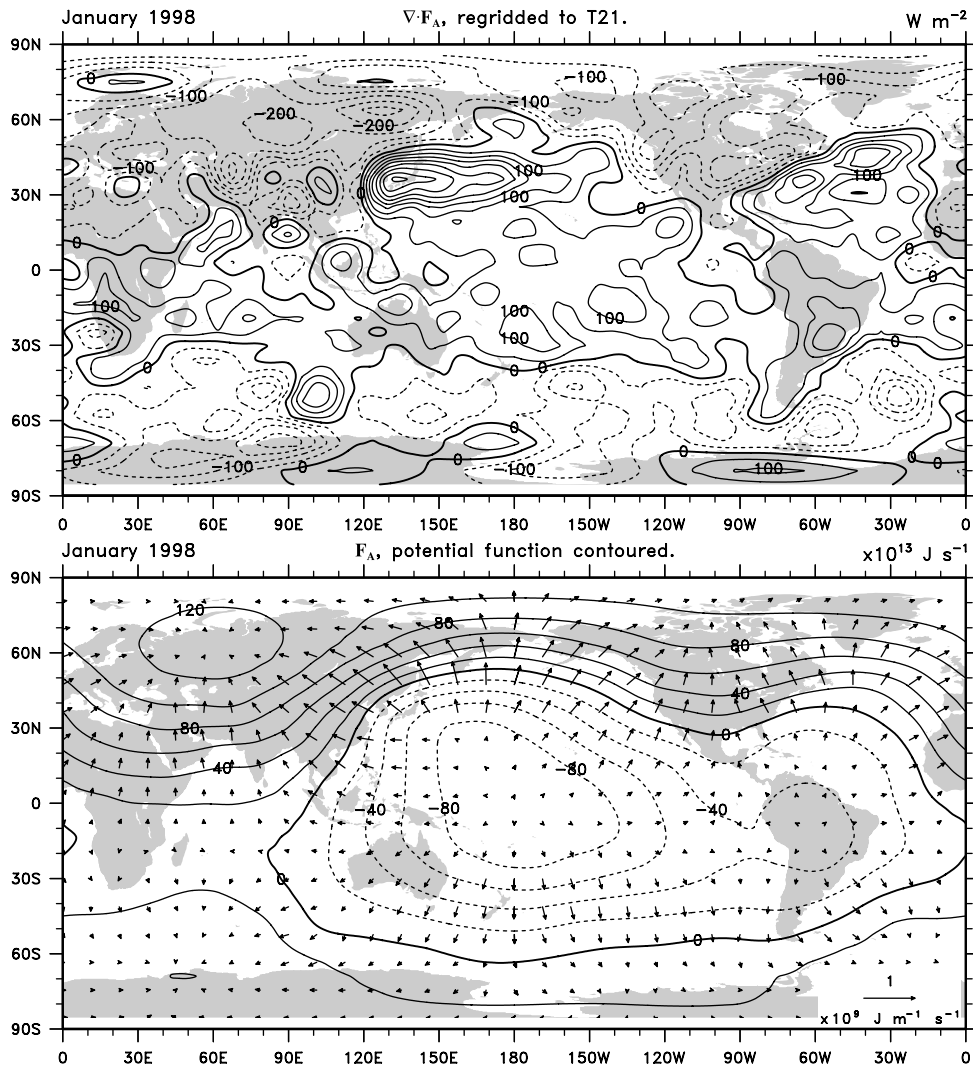


Figure 2. Total divergent vertically integrated energy transport and its divergence for January 1998, as in Figure 1. (Monthly mean and anomaly fields reflect regridded values; see Appendix A.)

[14] The SVD analysis can be performed using only part of a domain, and results can be projected to the rest of the domain using regression. Similarly, regression results can be derived for other fields to obtain associated correlative patterns. This is especially useful when essentially the same time series results for one field when combined in separate SVD analyses with several other fields, as is the case in the tropical Pacific.

3. An Example of Anomalous Atmospheric Energy Transports

[15] Figures 1 and 2 present summary results of the total divergent energy transport and its divergence $\nabla \cdot F_A$ for two different Januaries, January 1989 (Figure 1) and January 1998 (Figure 2), on the basis of the NCEP reanalyses. Figures 1 and 2 (bottom) show the actual vectors of the vertically integrated transport and its potential function, while Figures 1 and 2 (top) show the divergence. Similar results are obtained for the ECMWF reanalyses.

[16] The overall climatology of this data set has been documented and evaluated by Trenberth *et al.* [2001a]. However, to better appreciate the anomalous features seen in Figures 1 and 2, in Figure 3 for January we present the 20-year mean from 1979 to

1998, as well as the standard deviation of the anomalies. Figure 4 then shows the anomalies for January 1989 and January 1998.

[17] These two months also happen to be ones where we have some reliable data from the TOA. Using the ERBE base period of February 1985 to April 1989 to establish a climatology for each month, we compute anomalies for the TOA for January 1989 using the ERBE data and for January 1998 using CERES data for the tropics (see Figure 5). Anomalies are much greater in both the ASR and OLR fields (the latter are given in Figure 6) and exceed 50 $W\ m^{-2}$ in both years, but there is strong cancellation in their contribution to the net radiation. Differences are $<10\ W\ m^{-2}$ except in very small spots and in the stratocumulus cloud cover regions at $\sim 20^{\circ}\text{S}$ off the west coasts of Peru in the Pacific and Australia in the Indian Ocean. Therefore, because the changes in the net TOA fluxes are of the order of $<10\ W\ m^{-2}$, most of the field in Figure 4 arises from the net fluxes at the surface out of the ocean.

[18] These two months were chosen because they occur at times of the peak in the most recent El Niño event (Figure 2) and the major La Niña in 1988–1989 (Figure 1). The tropical Pacific will be discussed in more detail in section 4. For the moment, we note that in January 1989, when there was a strong cold dry tongue in the tropical eastern Pacific (Figure 6), the net atmospheric convergence is as much as $150\ W\ m^{-2}$, and so the implication is that

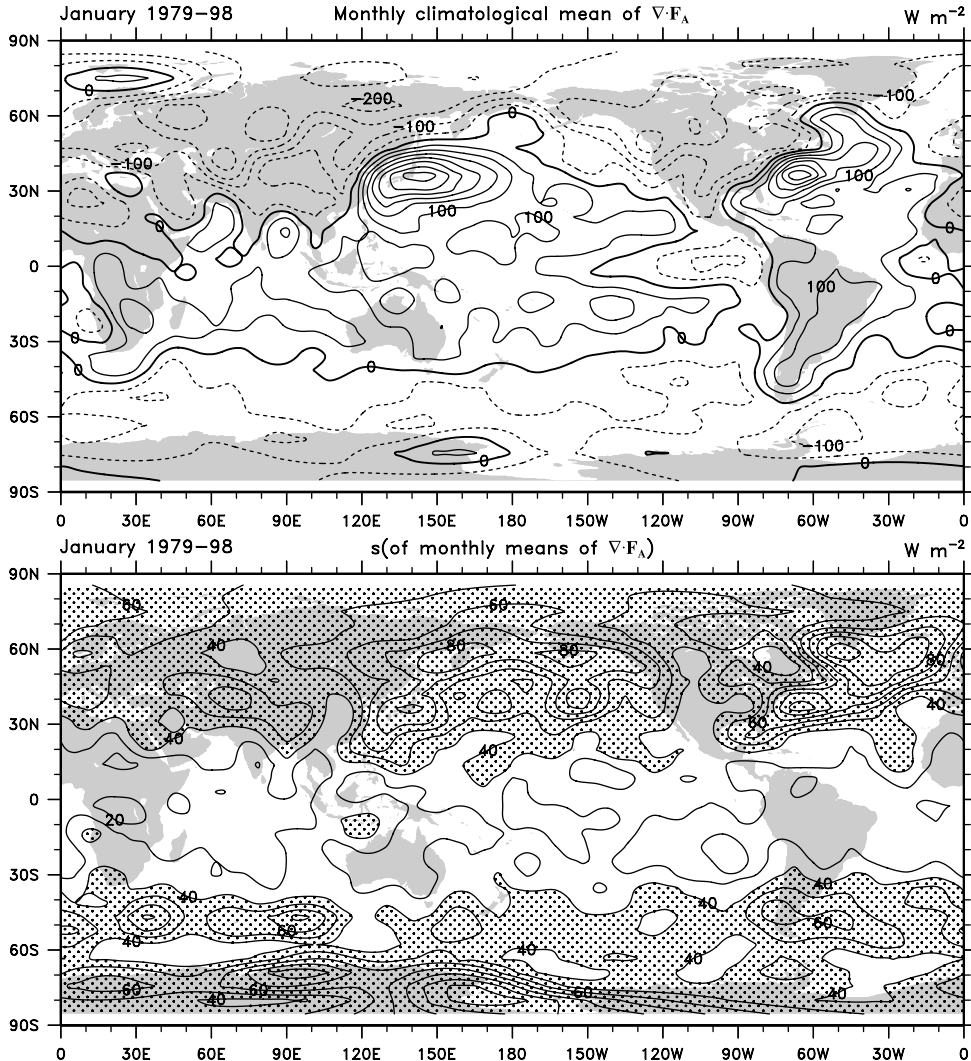


Figure 3. (top) Climatological mean for January 1979–1998 of the divergence of the vertically integrated atmospheric energy transport. Contour interval is 50 W m^{-2} . (bottom) Standard deviation of monthly anomalies. Contour interval is 10 W m^{-2} , and values exceeding 40 W m^{-2} are stippled. (Long-term means and standard deviations reflect regressed values; see Appendix A.)

the clear skies allow solar radiation to contribute to a strong heat flux into the ocean. In contrast, in 1998, under mature El Niño conditions, when the Intertropical Convergence Zone (ITCZ) and South Pacific Convergence Zone (SPCZ) were combined as extensive areas of convection over the equatorial Pacific (Figure 6), the net flux is mostly out of the ocean into the atmosphere. In terms of anomalies, the standard deviation of $\nabla \cdot F_A$ for January is $\sim 30 \text{ W m}^{-2}$ in the tropical Pacific (Figure 3), and the anomalies range from less than -70 W m^{-2} in January 1989 to $>70 \text{ W m}^{-2}$ in January 1998 (Figure 4).

[19] There was a strong reversal of the Pacific-North American (PNA) teleconnection pattern in the northern extratropics between these months. In January 1989 the PNA index anomaly was -1.5 standard deviations versus $+2.2$ standard deviations for January 1998 (see NOAA's monthly Climate Diagnostics Bulletin (available at www.cpc.ncep.noaa.gov/products/analysis_monitoring/bulletin) for definition and values). In January 1989, sea level pressure anomalies exceeded $+18 \text{ mbar}$ at 45°N , 180° in the Pacific, signifying a weak and split Aleutian low-pressure system. In contrast, during January 1998, there was a deep well-organized Aleutian low with a sea level pressure anomaly of -12 mbar . The result was a very different mean and transient flow out of Asia

into the Pacific. The huge differences in the surface fluxes (Figures 1 and 2) off Japan and over the Kuroshio extension region are a direct consequence of this. In January 1989 a broad region with heat fluxes into the atmosphere of $>100 \text{ W m}^{-2}$ peaked at just over 200 W m^{-2} , while in January 1998 the peak fluxes into the atmosphere for the monthly mean exceeded 350 W m^{-2} but the areal extent of the fluxes of $>100 \text{ W m}^{-2}$ was not as great. In both years the monthly anomalies in $\nabla \cdot F_A$ exceeded $\pm 75 \text{ W m}^{-2}$.

[20] Also of note in Figures 1 and 2 is the huge contrast in the Labrador Sea. The Icelandic low changed from $<990 \text{ mbar}$ in January 1989 to 1000 mbar in January 1998, and in January 1989, there was a $+15\text{-mbar}$ anomaly in sea level pressure over Europe. A strong positive NAO in January 1989 ($+2.0$ standard deviation anomaly) led to cold outbreaks over the northeast of Canada and Greenland and resulted in fluxes of $>250 \text{ W m}^{-2}$ out of the ocean in the Labrador Sea compared with a flux into the ocean in the same region in January 1998, when the NAO was weak (index $+0.1$). These anomalies exceeded $\pm 105 \text{ W m}^{-2}$ and are >1 standard deviation departures from the mean.

[21] Overall, the patterns seen here are reasonable. As January is the northern winter, when heat preferably goes into the southern

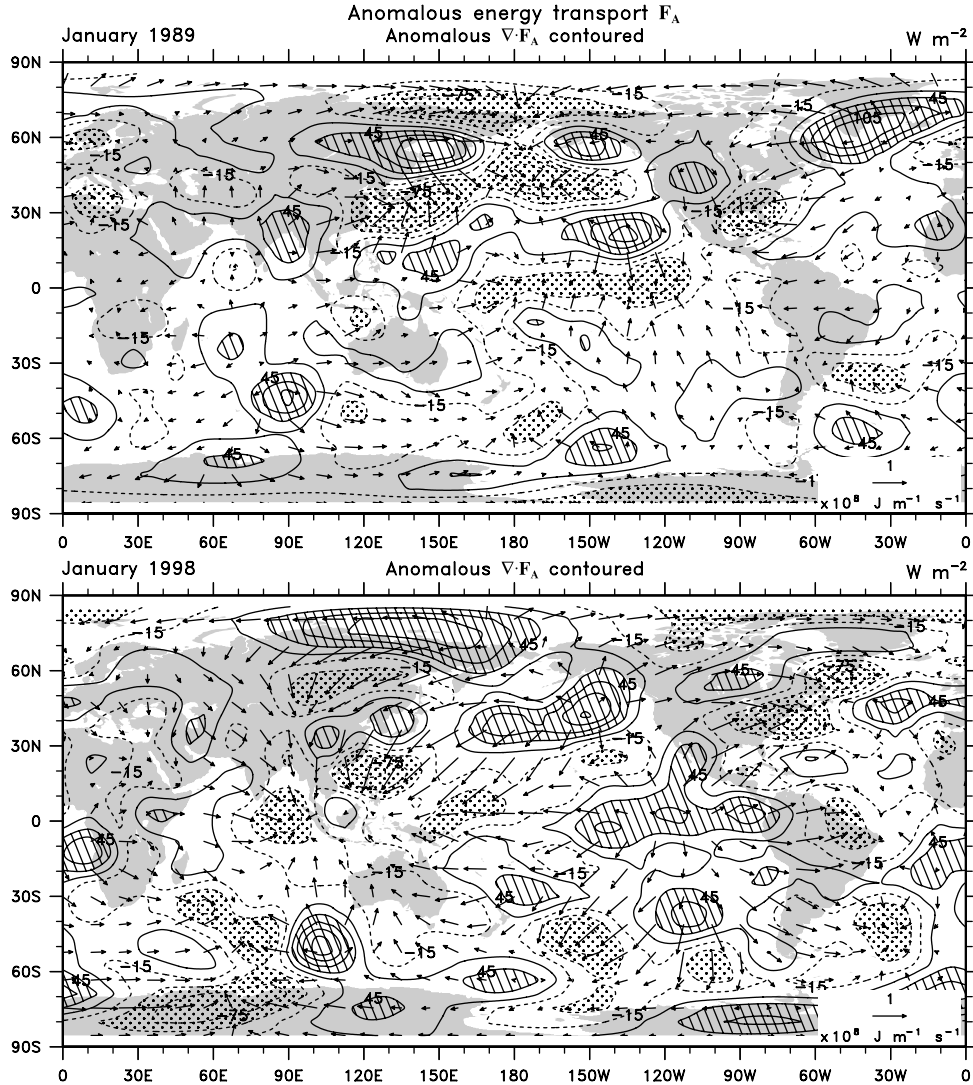


Figure 4. Anomalies of vertically integrated divergent energy transport (vectors) and their divergence for (top) January 1989 and (bottom) January 1998. Values exceeding $45 W m^{-2}$ are hatched, and values below $-45 W m^{-2}$ are stippled. Contour interval is $30 W m^{-2}$. (Monthly mean and anomaly fields reflect regressed values; see Appendix A.)

oceans and out of the northern oceans, following the sun, the main atmospheric transports are into the Northern Hemisphere. There is a strong land-sea contrast, as expected. A few unrealistic features show up, such as positive values over parts of the southern oceans and Antarctica that are not reproducible and that clearly relate to quality of the analyses.

4. Tropical Pacific Variability

[22] We have examined the evolution of the anomaly fields of the divergence of the atmospheric energy transports using movie loops and statistical analysis. Not unexpectedly, there is a very high level of “blinking” on and off of anomalies in individual months, and there are even switches in sign from month to month that are partly caused by the effects of individual synoptic systems. The presence of a warm sector in a region at the end of one month followed by the region behind the cold front of a cyclonic storm at the beginning of the next month leads to considerable weather-related noise, and part of the balance is with the local energy storage tendency terms. The magnitude of the noise is quite high in the extratropics and especially over Antarctica and the Southern

Oceans where the quality of the analyses is not as great [Trenberth et al., 2001a]. However, we are more interested in underlying systematic patterns that indicate the changes in storm tracks and climate influences of the ocean on the atmosphere. Accordingly, it proves to be desirable to smooth the monthly anomalies and suppress the very high frequency fluctuations from the analysis, as noted in section 2. While there remain considerable high-frequency fluctuations in $\nabla \cdot F_A$ in the extratropics, it proves not to be very coherent, and so the tropical regions dominate in an analysis of the covariability. However, this result may also have been preferred because we analyze anomalies for all months of the year concatenated, therefore not recognizing the seasonality of the extratropics.

4.1. Time Series of Niño 3.4 Region

[23] El Niño events tend to dominate the large-scale coherent patterns of divergent atmospheric energy transports, as will be shown below. Therefore, to set the stage for subsequent analyses, we present two key ENSO indices in Figure 7. These are the Southern Oscillation Index (SOI) based upon Tahiti and Darwin pressures and the SST anomalies in Niño 3.4 region ($170^\circ W -$

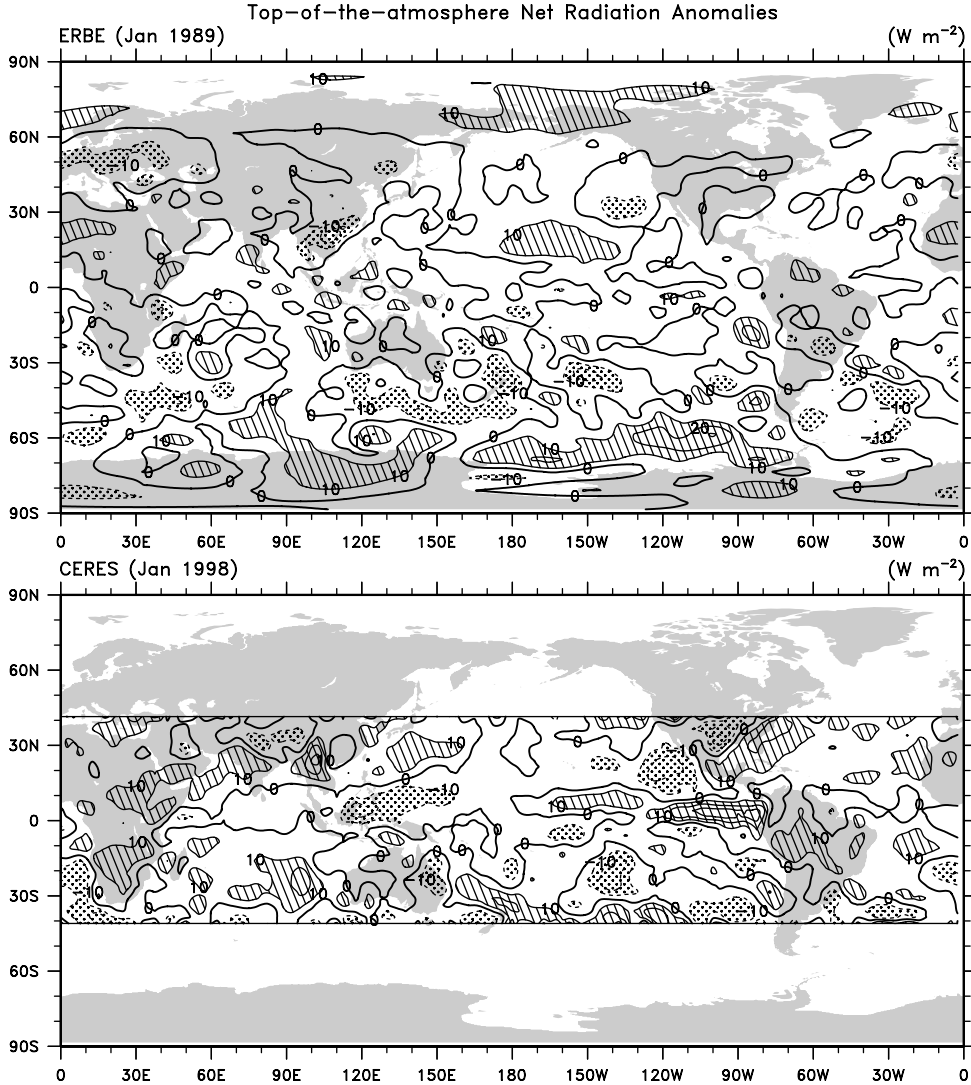


Figure 5. Anomalies in TOA net radiation in watts per square meter for January 1989 and January 1998. The base period is that from Earth Radiation Budget Experiment (ERBE), February 1985 to April 1989, and the Clouds and the Earth's Radiant Energy System (CERES) data in 1998 are restricted to $\pm 40^\circ$ latitude. Contour interval is 10 W m^{-2} , and values exceeding 10 W m^{-2} are either hatched (positive) or stippled (negative).

120°W , 5°N – 5°S), which we henceforth refer to as N3.4. (This shorthand is proposed to distinguish the SST anomaly area average over Niño 3.4 from area averages of other quantities over the same region). Higher than normal SSTs in this region go hand-in-hand with negative SOI values and signify an El Niño, while reversed signs indicate La Niña events.

[24] To further explore the atmospheric energy transports in the tropical Pacific, we average various quantities over the Niño 3.4 region. We present the vertically integrated divergence from both reanalyses, $\nabla \cdot \mathbf{F}_A$, as anomaly time series beginning in 1979 (Figure 8). The ECMWF reanalyses cover the period through 1993 only and, as noted by Trenberth et al. [2001b], suffer from spurious variability and two major discontinuities in the tropics in late 1986 and early 1989. In both cases, the tropical atmosphere, as analyzed, spuriously jumped to warmer values below 550 mbar and to cooler values above 550 mbar, adversely affecting the computations of the moist static energy. The whole time series is therefore somewhat corrupted, but it is shown to illustrate the extent of the agreement with NCEP values from the positive anomalies in 1982 to the negative anomalies in 1983 and to the positive anomalies again in 1986 of about the same magnitude. The time series from NCEP

clearly identifies all of the ENSO variability seen in Figure 7, with positive anomalies in $\nabla \cdot \mathbf{F}_A$ corresponding to the warm phase of the ENSO events.

[25] Anomalies in TOA radiation for the Niño 3.4 region are shown in Figure 9, all relative to the ERBE base period. The longest reasonably continuous time series related directly to radiation is that of OLR from the NOAA series of satellites. There is quite good agreement with the anomalies from ERBE (which used two of the same satellites) during the ERBE period, but there is not very good agreement with broadband measurements from Nimbus 7, which appears to show spurious drifts. Similarly, in 1998, there are disagreements and a positive offset between OLR measurements from CERES and those of NOAA, raising questions about both sets of data at these times. For net radiation the only reliable data are from ERBE, and relatively small variability in the Niño 3.4 region is evident with a range of $\sim 10 \text{ W m}^{-2}$. Nimbus 7 does provide a fairly long time series, although with a downward jump in 1980 that is likely spurious and with smaller variability over the common period. It nevertheless highlights the relatively small anomalies compared with those in Figure 8, which continue with the CERES data.

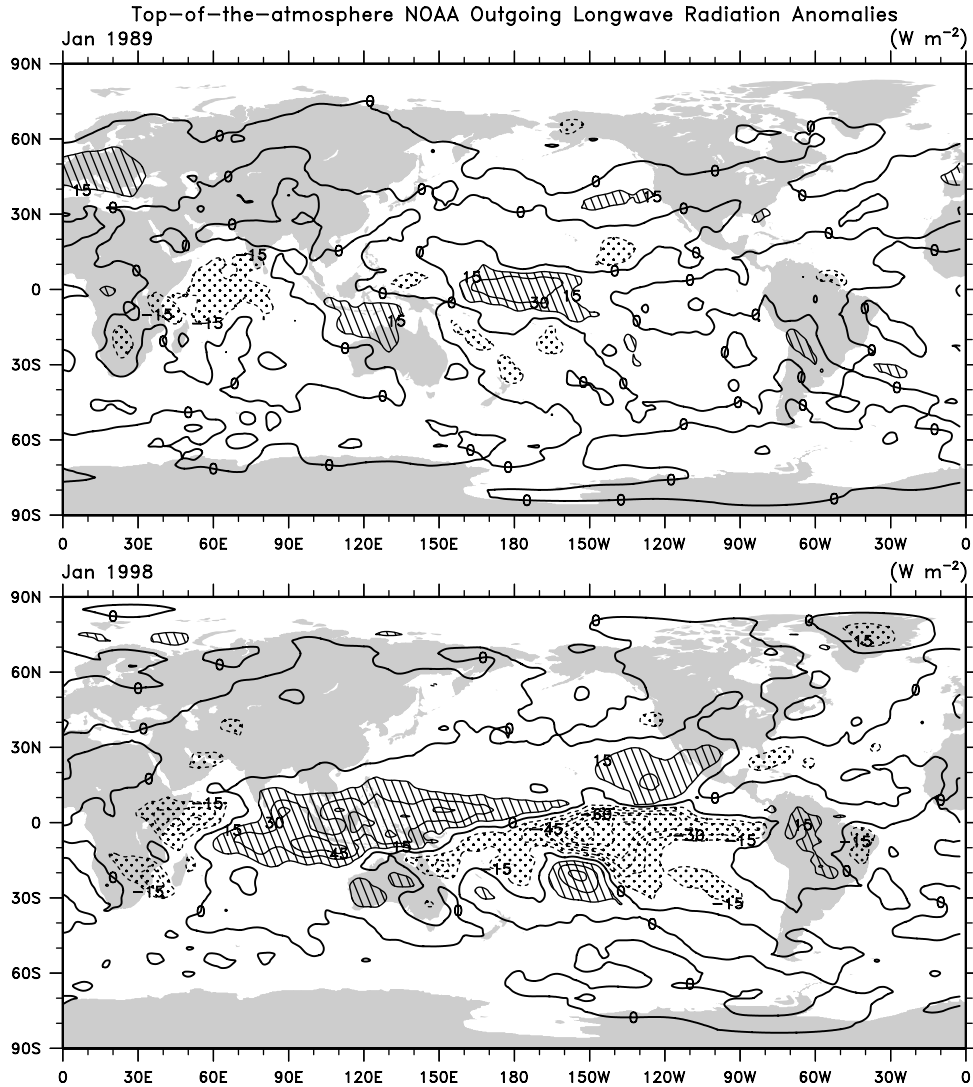


Figure 6. Anomalies in outgoing longwave radiation (OLR) in watts per square meter for January 1989 and January 1998 from National Oceanic and Atmospheric Administration (NOAA) satellites. Contour interval is 15 W m^{-2} , and values exceeding 15 W m^{-2} are either hatched (positive) or stippled (negative).

[26] We also examined averages of OLR over the more extensive region from 30°N to 30°S for systematic effects (Figure 10). As expected, there is a large cancellation within this region and, instead of the up to $\sim 50 \text{ W m}^{-2}$ values in Figure 9, the fluctuations

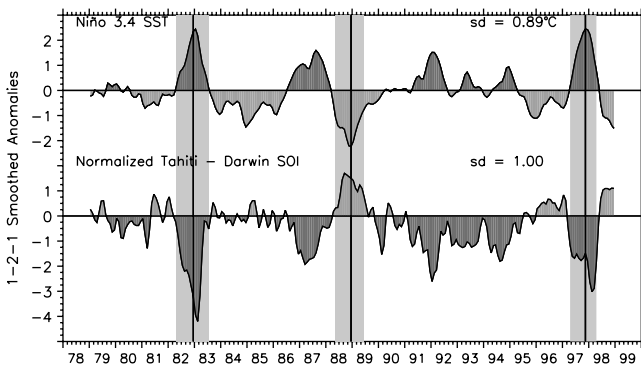


Figure 7. Time series of N3.4 and the Tahiti-Darwin Southern Oscillation Index. The three major events are shaded.

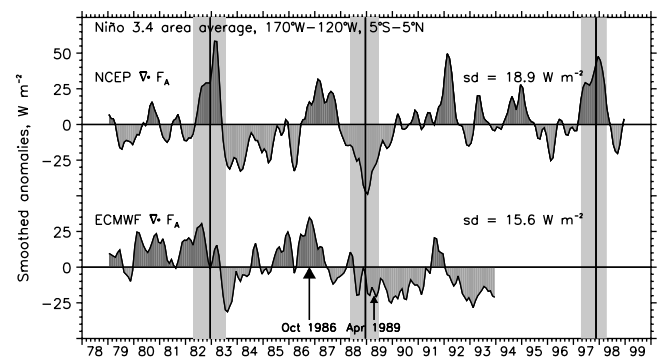


Figure 8. Anomalies in vertically integrated total energy divergence averaged over the Niño 3.4 region relative to the base period 1979–1993 in watts per square meter for (top) National Centers for Environmental Prediction/National Center for Atmospheric Research (NCEP/NCAR) and (bottom) European Centre for Medium-Range Weather Forecasts (ECMWF). Times of documented discontinuities in ECMWF are indicated.

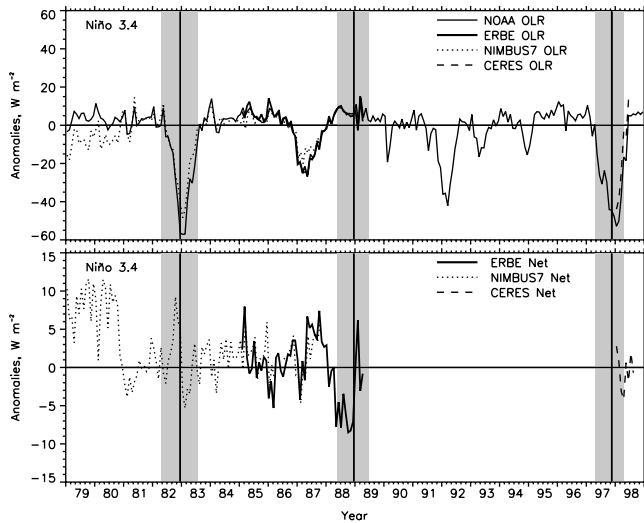


Figure 9. Anomalies in TOA radiation for the Niño 3.4 region. (top) Anomalies for OLR from the NOAA series of satellites adjusted for homogeneity (thin line), Nimbus 7 (dotted line), ERBE (thick line), and CERES (dashed line). Base period in each case is that of ERBE. (bottom) Net radiation from Nimbus 7, ERBE, and CERES, all relative to the ERBE base period.

are about $\pm 3 \text{ W m}^{-2}$. However, we conclude that rather than revealing real changes with time, most of what are present are spurious changes related to orbital changes in the satellites, among other things. In particular, from 1989 to early 1995, NOAA 11 drifted in orbit such that its local equator crossing time changed from 1400 to 1730, and it is exactly when NOAA 11 was replaced that the time series jumps back to anomalies near zero. This evidence shows that the Waliser [Waliser and Zhou, 1997] adjustments were insufficient to homogenize the series to better than $\sim 3 \text{ W m}^{-2}$, and this spurious drift is slightly worse in the original uncorrected OLR data. Also given in Figure 10 are the values for CERES in 1998 relative to the ERBE climatology, and these values immediately cast suspicion on their compatibility with the rest of the series. Issues that are related to these offsets are elaborated on by Duvel *et al.* [2001].

[27] Note that a 1°C temperature change over a column of water of 130 m depth over 5 months corresponds to a surface flux of $\sim 40 \text{ W m}^{-2}$. However, such a change over the Niño 3.4 region when redistributed throughout the 30°N – 30°S area amounts to $\sim 1 \text{ W m}^{-2}$ and is not measurable because it is less than the noise.

[28] The assessment of the net TOA measurements is that the interannual changes are most likely quite small and thus we can regard the atmospheric energy divergence as corresponding mostly to air-sea flux exchanges. However, we note the very strong resemblance between the NOAA OLR time series and the atmos-

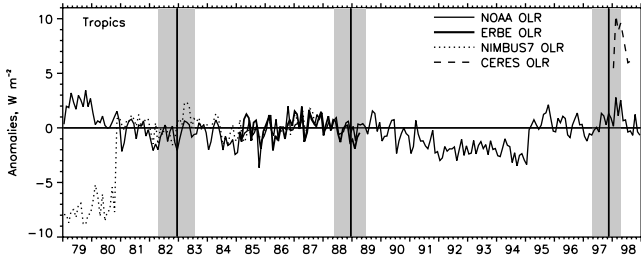


Figure 10. Anomalies in OLR averaged over the region 30°N – 30°S for Nimbus 7 (dotted line), ERBE (thick line), and CERES (dashed line). Base period in each case is that of ERBE.

Table 1. Contemporary Correlations of Monthly Time Series for 1979 to 1998 of SOI and Niño 3.4 Area Averages of SSTs, OLR, $\nabla \cdot \mathbf{F}_A$, and Precipitation

	SOI	SST	OLR	$\nabla \cdot \mathbf{F}_A$	Precipitation
SOI	1.0	-0.83	0.78	-0.76	-0.75
SST		1.0	-0.84	0.82	0.84
OLR			1.0	-0.76	-0.98
$\nabla \cdot \mathbf{F}_A$				1.0	0.77

pheric energy divergence in the tropical Pacific, and we note that these strongly resemble the indices of ENSO (Figure 7). Moreover, as these two data sets are entirely independent, the likelihood of these being chance relationships is very small. Contemporary correlations for the smoothed monthly anomalies among these indices are given in Table 1. All are very high, exceeding 0.75 in magnitude, and are highly statistically significant ($\alpha < 0.0001$). For correlations between variables with persistence related to ENSO [Trenberth, 1984] for the 240 months, this implies ~ 80 degrees of freedom and suggests statistical significance at the 5% level if the correlations exceed ~ 0.23 .

[29] The strong correlation between the tropical Pacific atmospheric energy divergence, and thus surface fluxes, arises primarily from the large ENSO events, revealed by the indices and shading in Figure 7. The areal extent of the Niño 3.4 region is $6 \times 10^{12} \text{ m}^2$, and thus the results of Trenberth *et al.* [2001a], which suggest random errors of $\sim 30 \text{ W m}^{-2}$ over 500-km scales, imply a random standard error of 6 W m^{-2} . This fits reasonably well with the coherence of the NCEP atmospheric energy divergence with the ENSO indices and strongly suggests that signals of $> 12 \text{ W m}^{-2}$ are significant. In the major El Niños over the Niño 3.4 region, the anomalies in 1982, 1986–1987, 1992, and 1997 all exceed 40 W m^{-2} , with the implied surface heat flux out of the ocean into the atmosphere. From there, heat is transported to higher latitudes and elsewhere in the tropics and subtropics. Large-scale overturning is the dominant process in the latter regions while, in the extratropics, many processes are involved as teleconnections alter storm tracks and advection by the flow [Trenberth *et al.*, 2002]. In 1982 and 1997, the biggest El Niño events, the anomalies exceed 60 W m^{-2} for a few months. In addition, in these events the areal extent of the anomalous fluxes is much greater than just the Niño 3.4 region. At the other extreme, with the La Niña events during this period, the anomalies are not quite as large, but they last a bit longer. In the Niño 3.4 region, for several months during mid-1983 to early 1986, anomalous heat fluxes into the ocean exceed 35 W m^{-2} , and during the 1988–1989 event the anomalous fluxes exceed 50 W m^{-2} for a few months.

4.2. SVD Analyses

[30] We performed several exploratory SVD analyses, using global domains as well as domains limited to the Pacific. We also explored results where one field was lagged relative to the other by ± 6 months. It was readily apparent that all results were dominated by ENSO events in the first two or three modes and that the evolution of ENSO necessitates more than one mode to explain the ENSO-related variability. Therefore, to focus the analyses on the Pacific, we have chosen to present results whereby the domain for the SVD analysis was restricted to that of the Pacific, although the results are not sensitive to this.

[31] The main SVD analysis results we present are between $\nabla \cdot \mathbf{F}_A$ and SST for the first two modes. Results for SST with CMAP precipitation produce the same time series and pattern for SST, and therefore we also present those results.

[32] Figures 11 and 12 present the homogeneous correlation patterns of SST and $\nabla \cdot \mathbf{F}_A$ for the first two modes, while Figure 14 presents the time series. The corresponding patterns for precipitation are shown in Figure 13, and the time series for the precipitation-SST SVD patterns are also given in Figure 14. For $\nabla \cdot \mathbf{F}_A$

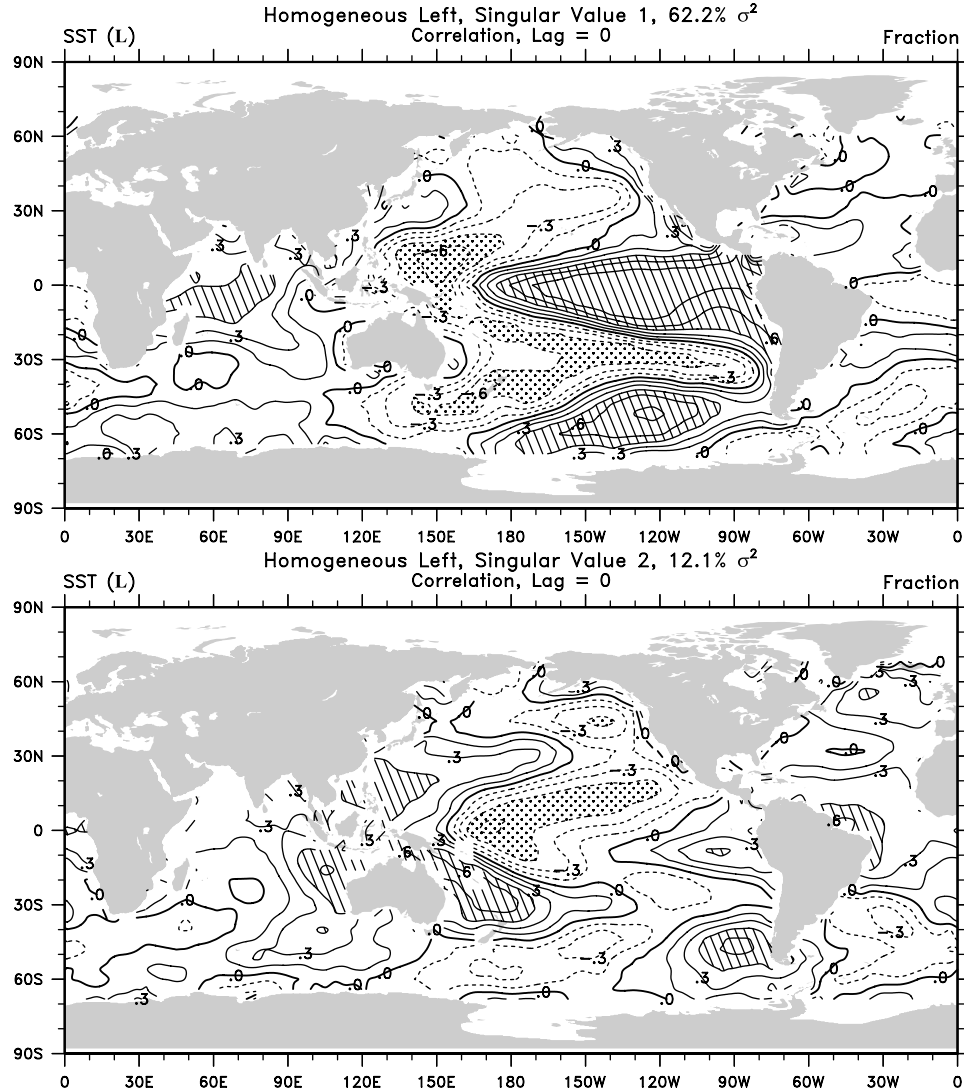


Figure 11. Correlation patterns of sea surface temperatures (SST) anomalies with the homogeneous time series of (top) singular value decomposition (SVD)1 and (bottom) SVD2. Contour interval is 0.15, and values exceeding 0.45 are either hatched (positive) or stippled (negative).

and SST the SCFs for the two modes are 62.2% and 12.1% of the covariance in the Pacific domain (versus 39.5% and 15.4% for the global domain analysis). The $\nabla \cdot \mathbf{F}_A$ and SST time series are correlated at 0.92 and 0.87 for the first two modes, and the maximum correlation is at zero lag. It is readily apparent that the time series of SVD1 are also highly correlated with ENSO indices, and for N3.4 the correlation is 0.90 for SST and 0.87 for $\nabla \cdot \mathbf{F}_A$. Of more interest is that the cross correlation is a maximum, with N3.4 leading the other time series by 2 months (correlations at 0.94 and 0.91, respectively). The precipitation time series are highly correlated with the others (0.93 with SST and 0.94 with $\nabla \cdot \mathbf{F}_A$) and in phase.

[33] While the time series from SVD2 are negatively correlated with N3.4 at zero lag of about -0.2 to -0.3 , the correlations are 0.40 and 0.43 (SST and $\nabla \cdot \mathbf{F}_A$) with SVD2 leading N3.4 by 10 months and -0.65 and -0.48 with N3.4 leading SVD2 by 7 months, strongly indicating the role of SVD2 in the evolution of ENSO. Thus SVD2 patterns with reversed sign occur some 10 months before SVD1, to be followed by SVD2 7 months later. For the 1979–1998 period, El Niño-related SST warming occurs first in the western/central equatorial Pacific and progresses eastward to develop later along the coast of South America. Hence this sequence relates to the times of change of SSTs in Niño 4 (near

the dateline) and Niño 1 and 2 (along the South American coast) regions (hereinafter referred to as 1 + 2), compared with those in the central tropical Pacific as given by SVD1 and N3.4. Accordingly, we have formed a new index that we call the Trans-Niño Index (TNI), given by $TNI = SST_{1+2N} - SST_{4N}$, where N refers to normalization by the standard deviation of the SST anomalies for each time series [Trenberth and Stepaniak, 2001]. The correlation of TNI with the SST SVD2 time series is 0.8. Because N3.4 equals $0.5[SST_{1+2N} + SST_{4N}]$, it has almost zero correlation at zero lag with TNI and thus is orthogonal. Hence the combination of N3.4 and TNI provides an efficient representation of ENSO through two different indices. The patterns associated with TNI are pursued by Trenberth and Stepaniak [2001].

[34] The spatial patterns of SST in SVD1 reveal the strongest relationship with the Niño 3.4 region. The anomaly in that region extends throughout the tropical central and eastern Pacific of one sign, with boomerang-shaped opposite-signed anomalies at 20° – 30° latitude in both hemispheres and in the far western equatorial Pacific. Positive values in the Indian Ocean, a weak dipole structure in the tropical Atlantic, negative values in the North Pacific and around New Zealand, and positive values in the southeast Pacific are all features associated with ENSO. Through-

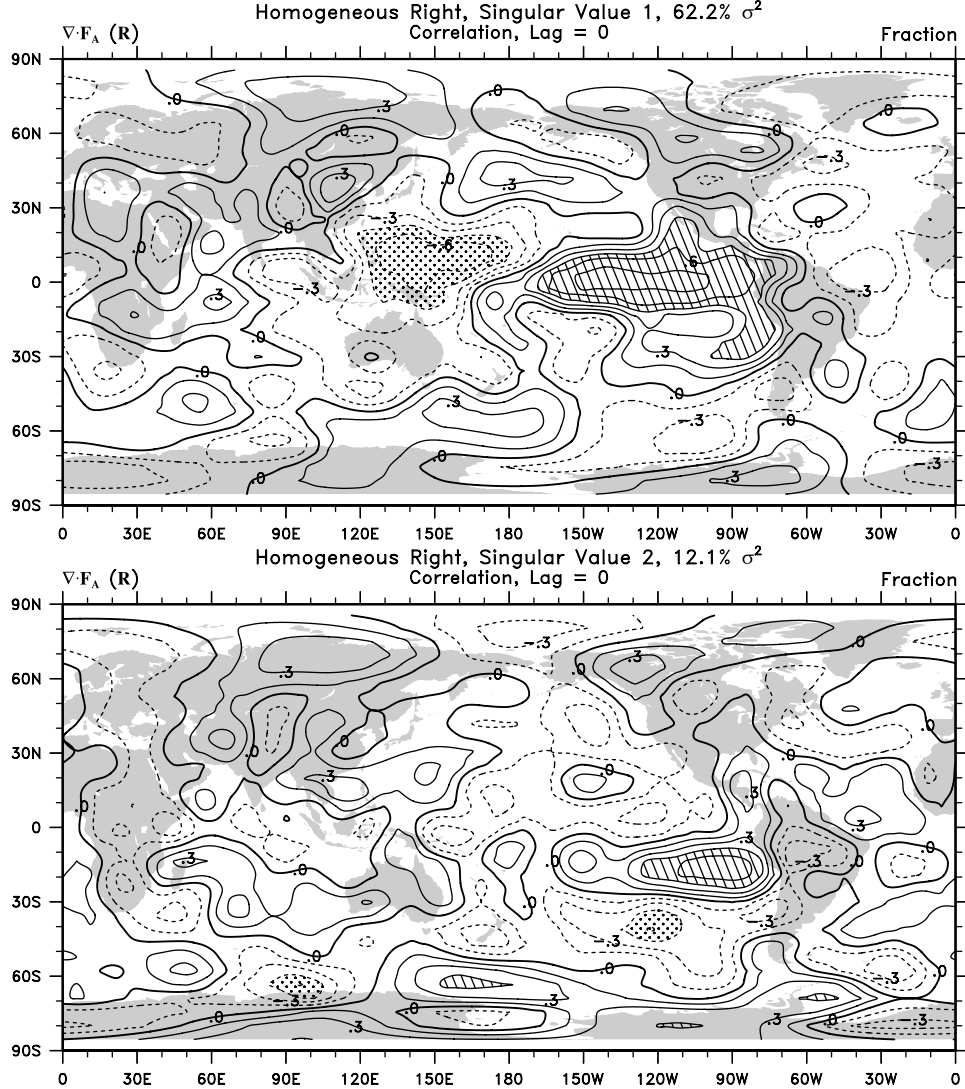


Figure 12. Correlation patterns of $\nabla \cdot \mathbf{F}_A$ anomalies with the homogenous time series of (top) SVD1 and (bottom) SVD2. Contour interval is 0.15, and values exceeding 0.45 are either hatched (positive) or stippled (negative).

out the tropics, there is a strong positive correlation with both the anomalies of associated precipitation and $\nabla \cdot \mathbf{F}_A$. Changes in precipitation depend upon the total field in which there is strong structure in the mean climatology, in particular the ITCZs and the SPCZ. Thus the dipole structure across 10°N in the Pacific is emphasized in the precipitation, but not SSTs, as the ITCZ moves south and the SPCZ moves northeastward with El Niño. The $\nabla \cdot \mathbf{F}_A$ is strongly related to both and seems to be in between, as is discussed next.

[35] To show the actual anomalies corresponding to a unit standard deviation of the SST time series for SVD1, Figure 15 presents the regression patterns for SST, precipitation, $\nabla \cdot \mathbf{F}_A$, and the vertically integrated diabatic heating. The latter is derived as a residual from the NCEP reanalyses [Trenberth et al., 2001a]. Anomalies in SST in the tropical Pacific slightly exceed 1.2°C and correspond to a peak of 2.5 mm day^{-1} in the precipitation anomaly farther to the west near 170°W on the equator and to $\sim 18 \text{ W m}^{-2}$ in $\nabla \cdot \mathbf{F}_A$ and, presumably, in the surface heat flux into the atmosphere. This would correspond to a surface evaporative rate of 0.6 mm day^{-1} . However, examination of results from the assimilating NCEP model integrations of the evaporation indicates only weak systematic associated evaporation anomalies of order 0.3 mm day^{-1} (not shown). For $\nabla \cdot \mathbf{F}_A$, anomalies just as large as in the

eastern tropical Pacific, but of opposite sign, occur in the tropical western Pacific north of the equator. Of course, for $\nabla \cdot \mathbf{F}_A$ the global mean has to be zero as the divergence of energy from one region shows up as convergence elsewhere. The diabatic atmospheric heating in Figure 15 reveals heating of 50 W m^{-2} in the N3.4 region and cooling in a boomerang-shaped region to the west.

[36] Similar relationships seem to hold for SVD2 in the tropics (not shown). However, the relationships among variables are quite different in the extratropics and in some parts of the tropical Atlantic. The positive correlations between SST and the other variables in the tropics in SVD1 patterns reverse in the North and South Pacific poleward of $\sim 30^\circ$. In these regions the evidence suggests that the atmosphere predominantly drives the ocean changes, so that a divergence of energy out of a region is associated with increased flux out of the ocean and colder SSTs, consistent with changes in the atmosphere arising from teleconnections (an atmospheric bridge) from the tropics [Lau and Nath, 1994; Trenberth et al., 1998].

5. Discussion

[37] Precipitation is a direct indicator of the latent heating in the atmosphere, and this is a substantial part of the tropical atmos-

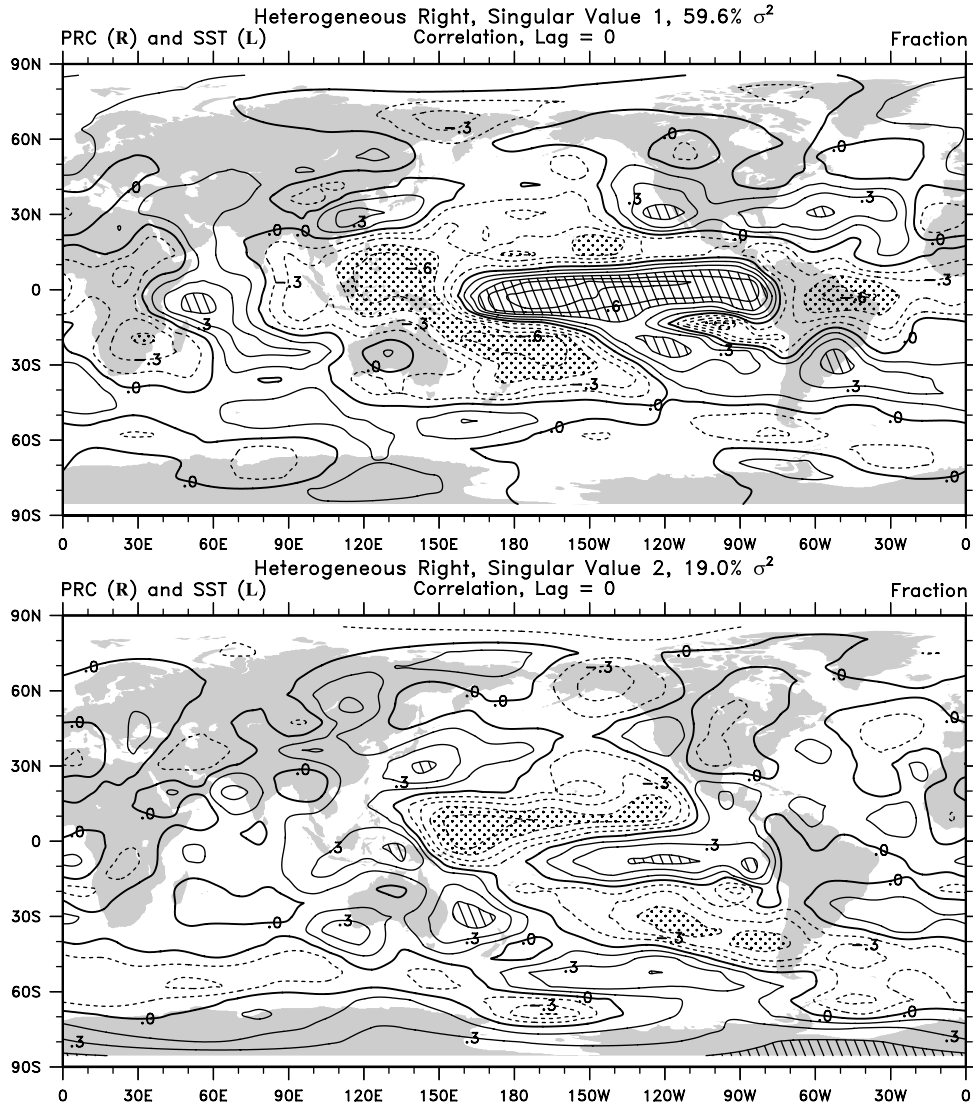


Figure 13. Associated heterogeneous correlation patterns of precipitation with the SST time series for (top) SVD1 and (bottom) SVD2. Contour interval is 0.15, and values exceeding 0.45 are either hatched (positive) or stippled (negative).

pheric diabatic heating. The diabatic heating is sometimes called Q_1 , and, ignoring a tiny frictional heating component, its vertical integral is given by

$$Q_1 = R_T + F_s + L(P - E), \quad (2)$$

where P is precipitation and E is evaporation in the column and L is the latent heat of vaporization. The term LE cancels a part of F_s , leaving the surface radiation and sensible heat flux. When this expression is compared with (1) for $\nabla \cdot \mathbf{F}_A$, the difference is the last term. Therefore Q_1 is not a driver of changes in moist static energy or total energy because changes in the state of moisture are internal and simply change the dry static energy at the expense of the moisture content as the convergence of moisture in the low levels is realized as latent heating. For this reason, there is a strong compensation between the dry static energy and the latent component.

[38] We have presented deduced covariability among a number of fields from several different data sets associated with ENSO. Qualitatively, the results make reasonable sense but quantitatively, several do not and are in fact inconsistent. *Trenberth and Guillemot*

[1998] evaluated the hydrological cycle in the NCEP reanalyses and concluded that the interannual variability in the tropical Pacific was much too weak (by about a factor of 2). Comparisons of precipitable water and precipitation from the reanalyses with other sources, such as the CMAP precipitation data set used here, suggest that this is the case. This also suggests that the variability in latent heating released in the atmosphere in the NCEP model is too low and it probably leads to underestimates of the diabatic heating. On the other hand, estimates of $\nabla \cdot \mathbf{F}_A$ are believed to be somewhat more robust owing to the cancellation of some errors in the moisture budget, as the moisture is converted into latent heating (see discussion of (2) above).

[39] There is further suspicion that the estimates of precipitation from CMAP underestimate the amounts in the central Pacific associated with El Niño. Alternative evidence from other precipitation estimates suggests that there should be a net positive precipitation anomaly, and thus latent heating anomaly, when averaged over the tropics associated with warm ENSO events [Soden, 2000]. Our results indeed suggest that there is large cancellation in OLR throughout the domain 30°N – 30°S , and, because precipitation estimates over the ocean are in large part

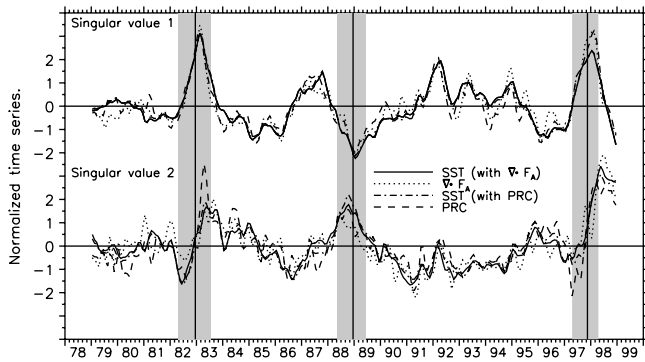


Figure 14. Time series from the SVD analyses for SST and $\nabla \cdot \mathbf{F}_A$ and for SST and precipitation for (top) SVD1 and (bottom) SVD 2. Major ENSO events are shaded as in Figure 7.

dependent on algorithms that use OLR and on passive microwave estimates that use assumptions based on other regions with regard to the melting level and other factors that come into play, this may be artificially built into the CMAP estimates.

[40] For the central tropical Pacific in warm ENSO events, from the regressions we would conclude that about a 1°C SST anomaly is associated with maximum rainfall anomalies of 2.5 mm day^{-1} , but this is suspected to be underestimated, as noted above. Even so, it corresponds to diabatic atmospheric latent heating of $>70 \text{ W m}^{-2}$, yet the indirect estimates from the NCEP reanalyses yield only 50 W m^{-2} . Similarly, estimates of evaporation from the NCEP reanalyses appear to be underestimates as they are at odds with the rainfall rates and with $\nabla \cdot \mathbf{F}_A$. However, patterns of evaporation with ENSO are complex as they depend upon not only air-sea temperature differences and relative humidity, but also wind speed (see Deser [1989] for an analysis of these dependencies and estimates of actual evaporation with ENSO events). Note that these estimates come from several different data sets, each with strengths but also with weaknesses, and the latter undermine a quantitative physically consistent picture.

[41] Nevertheless, in both SVD patterns in the tropics, positive SST anomalies are associated with increased heat flux into the atmosphere (presumably, mainly latent energy through surface evaporation, as found by Deser [1989]). In contrast, increased convective precipitation and decreased OLR occur in somewhat different locations governed by where the surface convergence occurs, and this depends on the mean precipitation patterns, the mean SST, and gradients in SST [Lindzen and Nigam, 1987]. The released latent energy forms a source and driver for the dry static energy, leading to a divergence of the atmospheric transports largely through large-scale overturning that is governed by the diabatic heating internal to the atmosphere, but does not relate well to surface fluxes.

[42] The implication is that the local surface flux of heat from the ocean to the atmosphere damps the SST anomaly, especially through evaporative surface heat fluxes that provide fuel for the precipitation. Transport of energy by the atmosphere occurs from regions of precipitation excess to regions of deficit, and the energy can most efficiently radiate to space in the clear-sky regions (as seen in the OLR). The alternative is that some energy is transported to higher latitudes by midlatitude baroclinic storms. The tropical transport of energy, however, also drives the transport of moisture from the evaporative sources to the precipitation sinks in the low-level return flow of the overturning circulation. The $\nabla \cdot \mathbf{F}_A$ is primarily related, through the associated surface fluxes, to the source of moisture, which is transported by the low-level atmospheric circulation and released as precipitation. To the extent that steady overturning dominates the circulation, then these two are directly linked through the driving by the diabatic heating, through

the latent heating in particular, and through the transport of the moisture to the regions where precipitation is realized.

[43] The positive correlations between $\nabla \cdot \mathbf{F}_A$ and SSTs in the tropical Pacific are reversed at higher latitudes and in some parts of

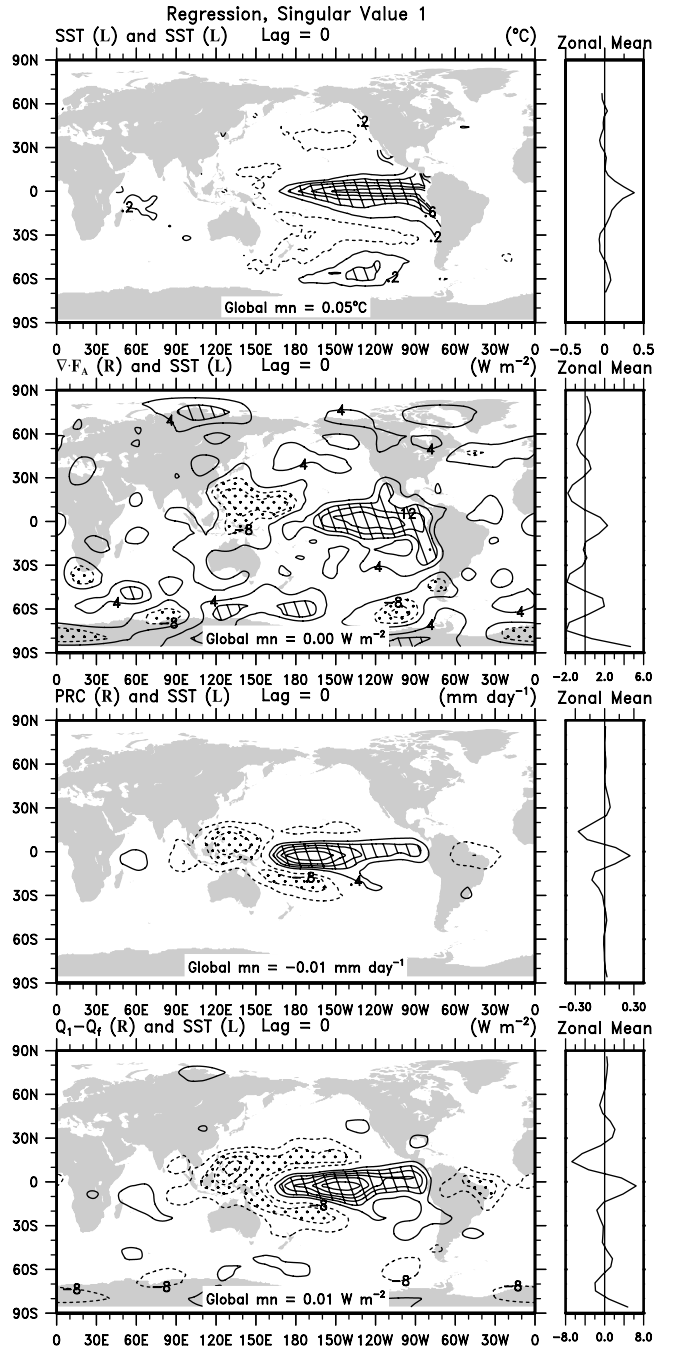


Figure 15. Regression patterns for SVD1 with the SST time series for (top to bottom) SST ($^\circ\text{C}$): contour interval is 0.2°C , and values exceeding 0.4°C are hatched; $\nabla \cdot \mathbf{F}_A (\text{W m}^{-2})$: contour interval is 4 W m^{-2} , and values exceeding 8 W m^{-2} are hatched (positive) or stippled (negative); precipitation: contour interval is 0.4 mm day^{-1} , and values exceeding 0.8 mm day^{-1} are hatched (positive) or stippled (negative); and atmospheric diabatic heating: contour interval is 4 W m^{-2} , and values exceeding 8 W m^{-2} are hatched (positive) or stippled (negative). The zero contour is omitted in all plots, negative values are dashed, and the zonal mean given at right.

the tropical Atlantic and Indian Oceans. A surprisingly strong pattern emerges over the South Pacific, although data are few in that region, and it seems to have a wave 2 structure that makes it similar in structure to the so-called Antarctic Circumpolar Wave [Peterson and White, 1998]. However, current evidence suggests that it is driven by ENSO and is mostly confined to the Pacific.

[44] Here we have outlined the contemporary relationships among several important climate variables. The evolution of ENSO and the implicit lag relationships manifested in the SVD1 and SVD2 patterns suggest that a systematic exploration of lead and lag relationships is warranted. However, the slow evolution of ENSO (as outlined, for instance, by Barnett *et al.* [1991] and Zhang and Levitus [1996]) is complex and expands the scope of this work to a point where it is necessary that these aspects should be pursued elsewhere [Trenberth and Stepaniak, 2001; Trenberth *et al.*, 2002].

6. Conclusions

[45] We used a case study that contrasted two different Januaries to illustrate the magnitude and importance of the variations from year to year in the atmospheric total heat or, more generally, in the energy budget. Examination of the corresponding top-of-the-atmosphere net radiative fluxes shows that it is primarily the surface fluxes from the ocean to the atmosphere that feed the divergent atmospheric transports. Anomalies in the extratropics in the surface fluxes between the ocean and atmosphere and the corresponding divergent energy transports within the atmosphere can exceed 120 W m^{-2} in individual months, especially where regime-like behavior, such as that associated with the NAO, prevails. More generally, synoptic activity in the atmosphere adds large high-frequency variability to the atmospheric transports and to the surface fluxes.

[46] In the tropics the variability is not as large in magnitude, but it extends over larger regions and is more persistent in time. A strong signal emerges in the atmospheric heat budget associated with ENSO, and during large El Niño events the anomalous divergence of the atmospheric energy transports exceeds 50 W m^{-2} over broad regions for several months. The evidence suggests that the ocean mainly drives the atmosphere in terms of thermal forcing. Ample evidence from many studies has, however, shown how the ocean is driven by the atmospheric winds in the tropics. The surface fluxes damp the SST anomalies, as first hinted at from sketchy observations and inferences about the latent heat flux by Weare [1984], and provide energy to drive the atmospheric circulation. Because a key component of the surface fluxes arises from evaporation, which moistens the atmosphere, the atmospheric response depends on where the moisture is converged and realized as latent heating thus driving the large-scale overturning in the atmosphere and transporting energy to the sink regions.

[47] The SVD analysis reinforces the primacy of ENSO as the dominant coupled mode of variability, as represented by time series of N3.4, although with clear evidence of the slow evolution of ENSO adding complexity. Changes in SST of $\sim 1^\circ\text{C}$ in the central and eastern Pacific correspond to changes in surface fluxes and atmospheric divergence of $\sim 20 \text{ W m}^{-2}$. More than double these amounts occur in major ENSO events, and thus surface flux anomalies of 50 W m^{-2} over extensive regions can result for several months, thereby accounting for much of the change in ocean heat content. However, the positive and negative regions in the atmospheric divergence have to balance, unlike the changes in SST. The negative feedback between SST and surface fluxes can also be interpreted as showing the importance of the discharge of heat during El Niño events and the recharge of heat during La Niña events. Relatively clear skies in the central and eastern tropical Pacific during La Niña allow solar radiation to enter the ocean, apparently offsetting the below-normal SSTs. Instead of warming the ocean locally the heat is carried away by ocean currents and Ekman transports and through adjustments

brought about by Rossby and Kelvin waves, and thus the heat is stored in the western tropical Pacific. This is not simply a rearrangement of the ocean heat, but also a restoration of heat in the ocean. Similarly, during El Niño the loss of ocean heat, especially through evaporation into the atmosphere, is a discharge of the heat content, and both contribute to the life cycle of ENSO. These observationally based conclusions support the picture put forward by Barnett *et al.* [1991] based mainly on model results in which the SST anomalies are created by ocean dynamics and the response to wind forcing, and not by local surface fluxes. However, these conclusions have been difficult to establish from observations, and quantitative aspects are still uncertain. Nevertheless, the role of the surface fluxes and the diabatic component of the ENSO cycle should not be underestimated.

[48] The exploration of the TOA energy budget exposes small but spurious changes in OLR of up to 5 W m^{-2} that appear to be associated with orbital drift and changes in equator crossing times of satellites that have yet to be adjusted for in the data sets. We also note that recent CERES results from TRMM are incompatible with earlier ERBE results and with those from the NOAA series of satellites. We further comment on the inconsistencies arising among the pictures of ENSO from the different data sets, which suggest that improved, more continuous and consistent observations and analyses are essential to make further progress.

[49] We have also exposed intriguing lead and lag relationships among the variables and time series, in particular between SVD 1 and SVD 2 and between both with N3.4. The evolution of ENSO necessitates more than one mode to explain the ENSO-related variability, a point often not adequately appreciated by a number of analyses that simply use one ENSO index to "remove" the effects of ENSO linearly from time series [e.g., Jones, 1989; Christy and McNider, 1994; Zhang *et al.*, 1996]. On the basis of SVD 2, we propose a second time series, TNI, as a simple second index important in the evolution of ENSO [Trenberth and Stepaniak, 2001]. Other aspects of the evolution are explored by Trenberth *et al.* [2002].

Appendix A

[50] Over a year after the original data processing for this study was completed, some problems were found in the NCEP reanalyses by NCEP that arose from moving software to new computers. The first problem was with the processing of TIROS Operational Vertical Sounder (TOVS) satellite data (information available at http://wesley.wwb.noaa.gov/tovs_problem/) in which unreliable data over land had been included erroneously in the analyses after March 1997. These analyses have been reprocessed and corrected by NCEP as of about mid-2001. Unfortunately, a second serious problem also occurred at NCEP, discovered in August 2001 (after the reviews of this paper were received), in which the values advertised as archived on the T62 Gaussian grid had inadvertently been switched to a regular latitude-longitude grid of the same dimension but with a header saying they were still on a Gaussian grid (information available at ftp://wesley.wwb.noaa.gov/pub/reanal/random_notes/grbsanl.txt). This affects the latitudes of the assigned values and creates location errors of as much as 1.4° latitude near the poles and 0.7° near 45° latitude, decreasing to nearly zero at the equator. Plotted on a global map, the fields look identical to the eye, but the small offsets and effective stretching of the grid lead to important differences in areas of large meridional gradients when the fields are differenced. For scalar fields the pole value is constant at all latitudes, and this suppresses wave structures at high latitudes if applied to a Gaussian grid. This problem also evidently began in March 1997.

[51] Because we used January 1998 as a case study in this paper, we were compelled to assess the impact of these errors on our results. Accordingly, we reprocessed the revised analyses to determine the effects independently for both errors. The error in

TOVS processing resulted in spotty small-scale changes in $\nabla \cdot \mathbf{F}_A$ with globally averaged RMS differences of 13.8 W m^{-2} . The error in gridding the data is much more substantial. It amounted to differences of $<25 \text{ W m}^{-2}$ equatorward of $\sim 60^\circ$ latitude but incurred differences in excess of 100 W m^{-2} near the poles. However, it also had little practical consequence as it mainly tended to shift features, and the revised result is smoother and contains less noise. The monthly mean and anomaly fields for January 1998 in Figures 2 and 4 are the corrected ones, and the long-term means and standard deviations in Figure 3 have also been corrected.

[52] **Acknowledgments.** This research was sponsored by NOAA Office of Global Programs grant NA56GP0247 and the joint NOAA/NASA grant NA87GP0105. We thank Bruce Wielicki for help with the CERES data. The National Center for Atmospheric Research is sponsored by the National Science Foundation.

References

- Barnett, T. P., M. Latif, E. Kirk, and E. Roeckner, On ENSO physics, *J. Clim.*, 4, 487–515, 1991.
- Bretherton, C. S., C. Smith, and J. M. Wallace, An intercomparison of methods for finding coupled patterns in climate data, *J. Clim.*, 5, 541–560, 1992.
- Christy, J. R., and R. T. McNider, Satellite greenhouse signal, *Nature*, 367, 325, 1994.
- Deser, C., Meteorological characteristics of the El Niño/Southern Oscillation phenomenon, Ph.D. thesis, Univ. of Washington, Seattle, 1989.
- Duvel, J.-P., et al., The ScaRaB-Resurs Earth radiation budget dataset and first results, *Bull. Am. Meteorol. Soc.*, 82, 1397–1408, 2001.
- Hurrell, J. W., and K. E. Trenberth, Global sea surface temperature analyses: Multiple problems and their implications for climate analysis, modeling and reanalysis, *Bull. Am. Meteorol. Soc.*, 80, 2661–2678, 1999.
- Jones, P. D., The influence of ENSO on global temperatures, *Clim. Monit.*, 17, 80–89, 1989.
- Kyle, H. L., A. Mecherikunnel, P. Ardanuy, L. Penn, and B. Groveman, A comparison of two major Earth radiation budget data sets, *J. Geophys. Res.*, 95, 9951–9970, 1990.
- Kyle, H., et al., The Nimbus Earth Radiation Budget (ERB) Experiment: 1975 to 1992, *Bull. Am. Meteorol. Soc.*, 74, 815–830, 1993.
- Lau, N.-C., and M. J. Nath, A modeling study of the relative roles of tropical and extratropical SST anomalies in the variability of the global atmosphere-ocean system, *J. Clim.*, 7, 1184–1207, 1994.
- Lindzen, R. S., and S. Nigam, On the role of sea surface temperature gradients in forcing low-level winds and convergence in the tropics, *J. Atmos. Sci.*, 44, 2418–2436, 1987.
- Peterson, R. G., and W. B. White, Slow oceanic teleconnections linking the Antarctic Circumpolar Wave with the tropical El Niño-Southern Oscillation, *J. Geophys. Res.*, 103, 24,573–24,583, 1998.
- Reynolds, R. W., and T. M. Smith, Improved global sea surface temperature analyses using optimum interpolation, *J. Clim.*, 7, 929–948, 1994.
- Rieland, M., and E. Raschke, Diurnal variability of the Earth Radiation Budget: Sampling requirements, time integration aspects and error estimates for the Earth Radiation Budget Experiment (ERBE), *Theor. Appl. Climatol.*, 44, 9–24, 1991.
- Smith, T. M., R. W. Reynolds, R. E. Livezey, and D. C. Stokes, Reconstruction of historical sea surface temperatures using empirical orthogonal functions, *J. Clim.*, 9, 1403–1420, 1996.
- Soden, B. J., The sensitivity of the tropical hydrological cycle to ENSO, *J. Clim.*, 13, 538–549, 2000.
- Stendel, M., J. R. Christy, and L. Bengtsson, Assessing levels of uncertainty in recent temperature time series, *Clim. Dyn.*, 16, 587–601, 2000.
- Trenberth, K. E., Signal versus noise in the Southern Oscillation, *Mon. Weather Rev.*, 112, 326–332, 1984.
- Trenberth, K. E., Using atmospheric budgets as a constraint on surface fluxes, *J. Clim.*, 10, 2796–2809, 1997.
- Trenberth, K. E., and J. M. Caron, Estimates of meridional atmosphere and ocean heat transports, *J. Clim.*, 14, 3433–3443, 2001.
- Trenberth, K. E., and C. J. Guillemot, Evaluation of the atmospheric moisture and hydrological cycle in the NCEP/NCAR reanalyses, *Clim. Dyn.*, 14, 213–231, 1998.
- Trenberth, K. E., and A. Solomon, The global heat balance: Heat transports in the atmosphere and ocean, *Clim. Dyn.*, 10, 107–134, 1994.
- Trenberth, K. E., and D. P. Stepaniak, Indices of El Niño evolution, *J. Clim.*, 14, 1697–1701, 2001.
- Trenberth, K. E., G. W. Branstator, D. Karoly, A. Kumar, N.-C. Lau, and C. Ropelewski, Progress during TOGA in understanding and modeling global teleconnections associated with tropical sea surface temperatures, *J. Geophys. Res.*, 103, 14,291–14,324, 1998.
- Trenberth, K. E., J. M. Caron, and D. P. Stepaniak, The atmospheric energy budget and implications for surface fluxes and ocean heat transports, *Clim. Dyn.*, 17, 259–276, 2001a.
- Trenberth, K. E., D. P. Stepaniak, J. W. Hurrell, and M. Fiorino, Quality of reanalyses in the tropics, *J. Clim.*, 14, 1499–1510, 2001b.
- Trenberth, K. E., J. M. Caron, D. P. Stepaniak, and S. Worley, The evolution of ENSO and global atmospheric surface temperatures, *J. Geophys. Res.*, 107, 10,1029/2000JD000298, in press, 2002.
- Waliser, D. E., and W. Zhou, Removing satellite equatorial crossing time biases from the OLR and HRC data sets, *J. Clim.*, 10, 2125–2146, 1997.
- Weare, B. C., Interannual moisture variations near the surface of the tropical Pacific Ocean, *Q. J. R. Meteorol. Soc.*, 110, 489–504, 1984.
- Wielicki, B. A., T. Wong, D. F. Young, B. R. Barkstrom, and R. B. Lee III, Differences between ERBE and CERES tropical fluxes: ENSO, climate change or calibration?, paper presented at Tenth Conference on Atmospheric Radiation, Am. Meteorol. Soc., Madison, Wis., 1999.
- Xie, P., and P. A. Arkin, Analyses of global monthly precipitation using gauge observations, satellite estimates, and numerical model predictions, *J. Clim.*, 9, 840–858, 1996.
- Xie, P., and P. A. Arkin, Global precipitation: A 17-year monthly analysis based on gauge observations, satellite estimates and numerical model outputs, *Bull. Am. Meteorol. Soc.*, 78, 2539–2558, 1997.
- Zhang, R.-H., and S. Levitus, Structure and evolution of interannual variability of the tropical Pacific upper ocean temperature, *J. Geophys. Res.*, 101, 20,501–20,524, 1996.
- Zhang, Y., J. M. Wallace, and N. Iwasaka, Is climate variability over the North Pacific a linear response to ENSO?, *J. Clim.*, 9, 1468–1478, 1996.

J. M. Caron, D. P. Stepaniak, and K. E. Trenberth, National Center for Atmospheric Research, P.O. Box 3000, Boulder, CO 80305, USA. (jcaron@ucar.edu; davestep@ucar.edu; trenbert@ncar.ucar.edu)